Two-Dimensional Ultrawideband Radar Imaging of a Target With Arbitrary Translation and Rotation

Takuya Sakamoto, *Member, IEEE*, and Toru Sato, *Member, IEEE*

Abstract—Indoor target detection and imaging technologies hold great interest for security surveillance systems. The ultrawideband (UWB) radar is promising because it can complement conventional camera-based systems. However, conventional UWB radar imaging systems are costly and impractical because they require large antenna arrays for acceptable resolution. This paper proposes a low-cost UWB radar imaging method using the motion of a target. The method employs five antennas for estimating the motion of a target, including its rotation, to obtain an image. Previous work deals only with a target in translation without rotation, which makes the method difficult to apply in practice. The proposed method, an extension of such previous methods, obtains an accurate image for an elliptical or distorted nonelliptical target with arbitrary translation and rotation. Numerical simulation and experimental results show that the proposed method is capable of accurately estimating motions and shapes.

Index Terms—Radar imaging, rotation, security system, target motion, ultrawideband (UWB) radar.

I. INTRODUCTION

RECENTLY, indoor security surveillance systems have attracted a great deal of attention because of increased threats from crime and terrorism. Target imaging technologies are critical for such systems. Ultrawideband (UWB) radar is a promising technology because of the advantages that it brings which are not found in conventional camera-based systems, such as accurate distance measurement. Although a number of proposed imaging methods have had good accuracy and resolution, most of these methods require large and costly antenna arrays and radio-frequency switches or bulky robotic scanning systems. For radar imaging, Jofre *et al.* [1] showed that the number of antennas has a large effect on image quality. This means that there is a lower bound for the number of antennas needed to obtain the required resolution. In fact, Leuschen and Plumb [2] and Yarovoy *et al.* [3] employed 50 and 13 antennas, respectively, for ground-penetrating radar imaging. Counts *et al.* [4] employed only six antennas, but also used mechanical antenna scanning. To obtain even better image quality, Masuyama and Hirose [5], Dehmollaian and Sarabandi [6], Yang and Fathy [7], and Zhuge *et al.* [8] employed 144, 61, 256, and 81 antennas, respectively. To realize a simple and cost-effective UWB radar system, a new technology is needed.

A novel approach to this problem has been proposed in recent years. To mitigate the measurement time caused by the need for sequential switching to select an antenna from a large array, a code-division multiple-transmission scheme [9] has been proposed to realize high-speed real-time imaging. Huang *et al.* [10] introduced compressive sensing to reduce the number of antennas. They reduced the total number of antennas from 51 to 10 while maintaining the same sidelobe level in the image.

Another UWB radar imaging method to reduce the required number of antennas has been proposed by Matsuki *et al.* [11]. This is based on the motion of the target rather than the large antenna arrays. This idea is similar to Inverse Synthetic Aperture Radar techniques [12], [13], because both employ the motion of the target to improve image quality. However, for our intended application, the problem is more complex, because the target is relatively close to the antennas. This shifts the scattering centers on the target surface, depending on the relative positions of the antenna and target. In addition, the target motion cannot be modeled as a simple function because it is basically arbitrary. The method in [11] has been shown to be effective, because the system can be simplified and produced at a lower cost than conventional large array-based systems. The method assumes that a target moves in an unknown orbit without rotating. However, this assumption is not always relevant, because a target can change its viewing angle depending on its direction of movement. Although some proposed methods compensate for rotation to improve image resolution [14], [15], these methods assume that the target in the far field for which a scattering center can be modeled as a fixed point. Because this paper aims to develop an imaging method for a target in the near field, the motion of the scattering center must be taken into account. This paper presents a UWB radar system with five antennas for simultaneous estimation of a target's shape, translation, and rotation. The performance of the proposed method is established using both numerical simulations and experimentation.

II. SYSTEM MODEL

A 2-D model is assumed for simplicity, and it is our objective to estimate a 2-D target shape under this assumption. A five-element linear antenna array is installed at fixed intervals of $\Delta x = 0.2$ m on a straight line, as shown in Fig. 1. This straight line could correspond to a wall or ceiling of a hallway. Typically, the problem could be the imaging of the cross section of a human body walking along the hallway.

Each antenna is connected to a UWB pulse generator and a receiver and is operated as a monostatic radar system with
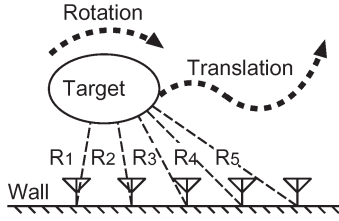
Fig. 1. Assumed system model.

modulation to avoid interference with other antennas. Any modulation can be used here as long as they are orthogonal to each other to realize a type of multiple-access system. Pulses are simultaneously transmitted from each antenna at time intervals of Δt, and echoes are received at the same antenna. The imaging methods proposed in this paper employ only the delay time of the echoes, which means it is essential to have an accurate ranging capability. The transmitted waveforms should satisfy this condition.

The target is assumed to have an unknown boundary $(X_0(\xi), Y_0(\xi))$, where $0 \leq \xi \leq 2\pi$ is a parameter. The centroid of the target is at the origin of the assumed coordinates. Under this condition, we can define rotation around the origin independently of the shape of the target. The target moves with a translation $(X_T(t), Y_T(t))$ and a rotation $\phi(t)$ with time t. The target boundary $(X(\xi, t), Y(\xi, t))$ at time t is determined by

$$\begin{bmatrix} X(\xi, t) \\ Y(\xi, t) \end{bmatrix} = R(\phi(t)) \begin{bmatrix} X_0(\xi) \\ Y_0(\xi) \end{bmatrix} + \begin{bmatrix} X_T(t) \\ Y_T(t) \end{bmatrix} \quad (1)$$

where $R(\phi)$ denotes a rotation matrix given by

$$R(\theta) = \begin{pmatrix} \cos\theta & -\sin\theta \\ \sin\theta & \cos\theta \end{pmatrix}. \quad (2)$$

The distance between each antenna and the scattering center of the target is measured as $R_i(t)$ $(i = 1, 2, \ldots, 5)$ using the ith antenna at each time step $t_n = n\Delta t$. The purpose of this paper is to develop a method to estimate the translation $(X_T(t), Y_T(t))$, rotation $\phi(t)$, and the target shape $(X_0(\xi), Y_0(\xi))$ using the range data $R_i(t)$ $(i = 1, 2, \ldots, 5)$.

III. PROPOSED METHOD

Matsuki *et al.* [11] proposed a method for estimating the translational motion and shape of a target, based on a fitting method using a circle. Because a circle has 3 DOFs, three antennas were used. However, this method cannot estimate the target's rotation because of the symmetry of a circle. We propose a new method using an ellipse rather than a circle to estimate both the rotation and the translation to obtain a target image.

A. Motion Estimation by Optimization With an Elliptical Shape Model

The proposed method estimates a local target shape for each time step $t = t_n$ using an elliptical model with five parameters

$a, b, x_0, y_0,$ and θ. The ellipse is expressed as follows:

$$\left(\frac{\cos^2\theta}{a^2} + \frac{\sin^2\theta}{b^2}\right)(x - x_0)^2 + \left(\frac{\sin^2\theta}{a^2} + \frac{\cos^2\theta}{b^2}\right) \times$$
$$(y - y_0)^2 + \sin 2\theta \left(\frac{1}{a^2} - \frac{1}{b^2}\right)(x - x_0)(y - y_0) = 1 \quad (3)$$

where a and b are the long and short axes of the ellipse, (x_0, y_0) is the center of the ellipse, and θ is the rotational angle. The distance between the ith antenna and the corresponding scattering center $c_i(a, b, x_0, y_0, \theta)$ is defined as $r_i(a, b, x_0, y_0, \theta)$. These variables c_i and r_i are calculated using the ith antenna position x_i. The scattering center $c_i(a, b, x_0, y_0, \theta)$ is equivalent to the point on the ellipse that is closest to the antenna x_i because there is no point closer to the antenna than the foot of a perpendicular on such a convex curve.

We define a cost function

$$F_n(a, b, x_0, y_0, \theta) = \sum_{i=1}^{N_a} |r_i(a, b, x_0, y_0, \theta) - R_i(t_n)|^2 \quad (4)$$

where $N_a = 5$ is the number of antennas. By minimizing this cost function, we determine the most likely parameter set of an ellipse using

$$(a_n, b_n, x_{0n}, y_{0n}, \theta_n) = \arg\min F_n(a, b, x_0, y_0, \theta). \quad (5)$$

To carry out this optimization process, the scattering center points $c_{n,i}$ $i = 1, 2, \ldots, 5$ for each time step $t = t_n$ must be calculated. To calculate these scattering centers, the optimized parameters $(x_{0n}, y_{0n}, a_n, b_n, \theta_n)$ and each antenna position x_i are used. The scattering center point $c_{n,i}$ is estimated as the foot of the perpendicular drawn through the ith antenna position. This process can be computed analytically, as detailed in the Appendix. The Levenberg–Marquardt algorithm is used to optimize (5) using the analytical expression for the scattering centers. The Levenberg–Marquardt algorithm is known to be fast and stable for minimization problems if the optimum cost function value is close to zero [16]. We call the motion estimation method proposed here the *one-step optimization method*, in contrast to the methods discussed next.

B. Stabilized Optimization With Fixed Parameters of the Elliptical Shape Model

We modify the optimization scheme presented in the previous section to stabilize the optimization process. Previously, we dealt equally with the five parameters a, b, x_0, y_0, and θ. However, they can be treated differently because they have different physical meanings. The key point is that a and b are related to the target shape, while the others are related to its motion. Using these characteristics, we introduce a smoothing process for a and b. We independently estimate the other parameters x_0, y_0, and θ at each time step with no smoothing.

The proposed optimization procedure for a and b is expressed as

$$(\hat{a}, \hat{b}) = \arg\min_{(a,b)} \sum_{n=0}^{N_{\mathrm{obs}}} \min_{(x_0, y_0, \theta)} F_n(a, b, x_0, y_0, \theta) \quad (6)$$

where N_{obs} is the total number of time steps for which the observed data are analyzed. The parameters (a, b) are estimated using the quasi-Newton method. For each (a, b), the remaining parameters (x_0, y_0, θ) are optimized using the Levenberg–Marquardt algorithm.

The model assumes the fixed parameters a and b throughout the data set, which does not necessarily mean that the target is modeled as an ellipse because the estimated motion is compensated for to obtain the final image, as explained in later sections. The optimization is stabilized because the number of degrees of freedom is reduced from five to three for (x_0, y_0, θ). We call this motion estimation method the *two-step optimization method with fixed shape parameters*.

If the target shape is close to an ellipse, the method works well for stabilizing the optimization by averaging the data in terms of time. The method, however, cannot be applied to a target that is distorted from an ellipse. In this case, this optimization must be extended, as described in the next section.

C. Stabilized Optimization With Time-Varying Parameters of the Elliptical Shape Model

To extend the optimization, we use the procedure

$$(\hat{a}_m, \hat{b}_m) = \arg\min_{(a,b)} \sum_{n=m-M/2}^{m+M/2} \min_{(x_0, y_0, \theta)} F_n(a, b, x_0, y_0, \theta) \quad (7)$$

which means that a and b are fixed during a finite period $m - M/2 \leq n \leq m + M/2$ while the other parameters are optimized at each time step. Here, M is a fixed value corresponding to the period for which the data are averaged to determine one set of a and b.

After calculating $\hat{a}_m$ and $\hat{b}_m$, these time series are smoothed using a Gaussian filter as follows:

$$\bar{a}_m = \frac{\sum_{\Delta m} \hat{a}_{m+\Delta m} \exp(-\Delta m^2 \Delta t^2 / 2\sigma^2)}{\sum_{\Delta m} \exp(-\Delta m^2 \Delta t^2 / 2\sigma^2)} \quad (8)$$

and the smoothed $\bar{b}_m$'s are calculated similarly. Finally, these smoothed values $\bar{a}_m$ and $\bar{b}_m$ are used for each time step to optimize the remaining parameters x_{0n}, y_{0n}, and θ_n using the Levenberg–Marquardt algorithm

$$(x_{0n}, y_{0n}, \theta_n) = \arg\min_{(x_0, y_0, \theta)} F_n(a_n, b_n, x_0, y_0, \theta) \quad (9)$$

where a_n and b_n are set by

$$(a_n, b_n) = \begin{cases} (\bar{a}_{L_1}, \bar{b}_{L_1}) & (n < L_1) \\ (\bar{a}_n, \bar{b}_n) & (L_1 \leq n \leq L_2) \\ (\bar{a}_{L_2}, \bar{b}_{L_2}) & (n > L_2) \end{cases} \quad (10)$$

where $L_1 = M/2$ and $L_2 = N_{\text{obs}} - M/2$. For n in both ends $n < L_1$ and $n > L_2$, there are inadequate numbers of data samples to be smoothed using (8). Therefore, we use the available smoothed parameters $(\bar{a}_{L_1}, \bar{b}_{L_1})$ and $(\bar{a}_{L_2}, \bar{b}_{L_2})$ at $m = L_1$ and $m = L_2$.

These three parameters $(x_{0n}, y_{0n}, \theta_n)$ are used as the estimated translational and rotational motions as in the previous section. We call this revised motion estimation method the *two-step optimization method with variable shape parameters*. These three proposed methods are compared in the following sections.

D. Phase Ambiguity in Estimating Rotational Motion

The parameters (x_0, y_0) and θ correspond to the translation and rotation of the target. Note that θ has ambiguity with integer multiples of π. All models expressed with $\theta + m\pi$ are identical, where m is an arbitrary integer. Because of this ambiguity, an estimated rotational motion can have discontinuities, making it difficult to estimate the rotation accurately. Consequently, we select the rotational angle that is closest to the previously estimated angle using

$$m = \arg\min |\theta_n - \theta_{n-1} + m\pi| \quad (11)$$

where θ_n is the estimated rotational angle at time t_n, thus minimizing the gap between two adjacent angles. We then update θ_n from $\theta_n \leftarrow \theta_n + m\pi$ to estimate the rotation.

E. Imaging Process by Compensating for Target Motion

The target shape is obtained from the target motion estimated using the procedure described in the previous sections. The image is estimated from the scattering centers by compensating for the motion. The scattering centers are used because the elliptical model approximates the target shape locally around the scattering centers and it is not relevant to use the entire elliptical shape estimated from the optimization process. Note that the scattering centers have already been calculated in (5) because $r_i(a, b, x_0, y_0, \theta)$ corresponds to the distance between a scattering center $\boldsymbol{c}_{n,i}$ and an antenna position $\boldsymbol{x}_i$. The next step is to compensate for (x_0, y_0) and θ to estimate the target shape at the initial state $t = 0$ using

$$\begin{bmatrix} \hat{X}_0^{(n,i)} \\ \hat{Y}_0^{(n,i)} \end{bmatrix} = R(-\theta_n) \left(\boldsymbol{c}_{n,i} - \begin{bmatrix} x_{0n} \\ y_{0n} \end{bmatrix} \right). \quad (12)$$

IV. PERFORMANCE EVALUATION USING NUMERICAL SIMULATION

A. Application to an Elliptical Target

We set the actual shape parameters $a = 0.15$ m, $b = 0.10$ m, and $\theta = -\pi/4$ rad. The translation is given by

$$X_T = X_0 + v_x t, \quad (13)$$

$$Y_T = Y_{T0} + Y_{Ts} \sin(\omega_0 t + \chi_0) \quad (14)$$

and the rotation is given by

$$\phi(t) = \phi_0 \sin(\omega_\phi t) \quad (15)$$

where $X_0 = -0.4$ m, $v_x = 2.0$ m/s, $Y_{T0} = 0.5$ m, $Y_{Ts} = 0.1$ m, $\omega_0 = 2\pi$ rad/s, $\chi_0 = \pi/3$ rad, $\phi_0 = 1.3\pi$ rad, and $\omega_\phi = \pi$ rad/s. The sampling interval is set at $\Delta t = 5.0$ ms.
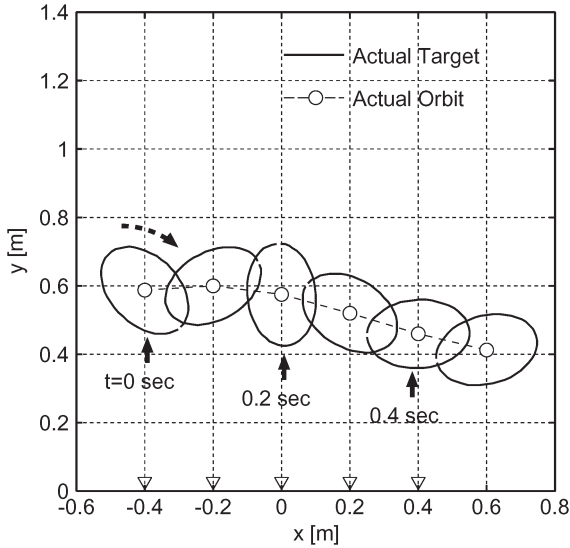
Fig. 2. Assumed elliptical target shape and motion with rotation.
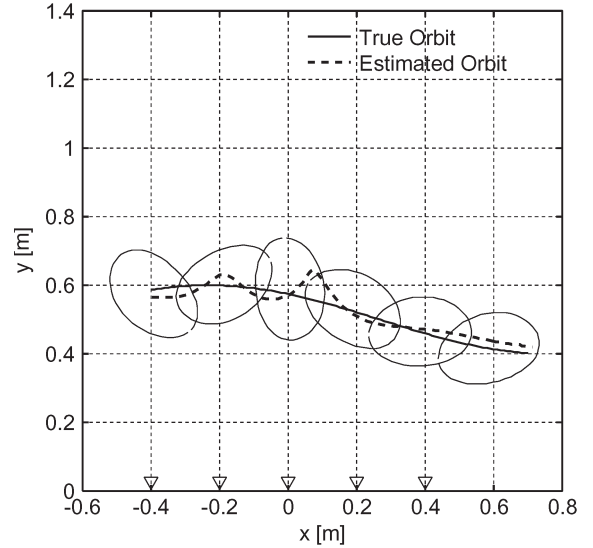

Fig. 4. Actual and estimated translation orbits using the one-step optimization method for nonelliptical target ($\delta = 0.1$).
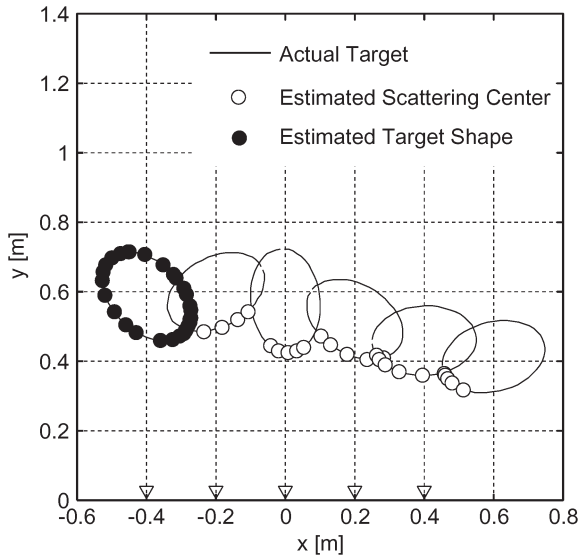

Fig. 3. Estimated scattered points and target shape for an elliptical target.

Fig. 5. Actual and estimated rotation angles with the one-step optimization method ($\delta = 0.1$).

Fig. 2 shows an elliptical target moving to the right and rotating clockwise. The solid lines and white circles in this figure provide snapshots of the target and its actual center positions. The five triangles on the x-axis represent the antenna positions. Note that the target boundaries are drawn every 100.0 ms purely for clarity, although the actual sampling interval is 5.0 ms. Some of the following figures are drawn in the same way.

Here, we demonstrate the results of applying the one-step optimization method. The white dots in Fig. 3 indicate the estimated scattering centers $c_{n,i}$, which are accurately located on the actual target boundaries (solid lines). These scattering centers are calculated with the parameters optimized in (5) at each time step. These points are transformed to the initial positions at $t = 0$ by compensating for the motion using (12) to finally obtain the target image as black dots in Fig. 3. The target shape is accurately estimated using the proposed method. This is because the actual target shape is elliptical, which is identical to the assumed elliptical model. The two-step optimization method gives a similarly accurate imaging result in this case.
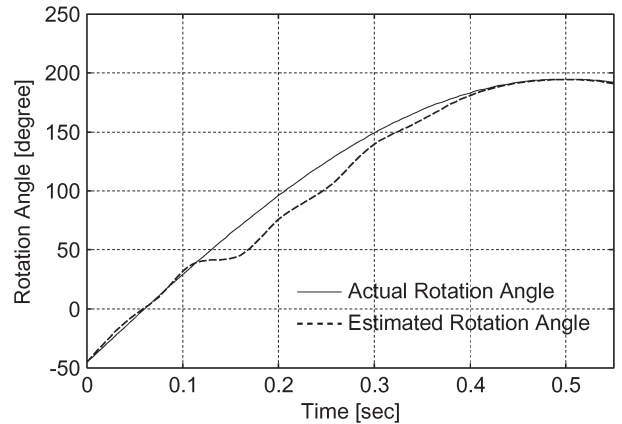
B. Application to a Slightly Distorted Nonelliptical Target

1) Distorted Target Model: We now investigate the performance of the proposed methods for a nonelliptical target. We assume a target shape expressed as follows:

$$\begin{bmatrix} X_0(\xi) \\ Y_0(\xi) \end{bmatrix} = \begin{bmatrix} a(1 + \delta \cos \xi) \cos \xi \\ b(1 + \delta \cos(\xi + \pi/4)) \sin \xi \end{bmatrix}. \quad (16)$$

The target shape is distorted from an ellipse as δ is increased, where $\delta = 0$ corresponds to the elliptical model dealt with in the previous section. The assumed target motion in the following sections is the same as in the previous section.

2) Applying One-Step Optimization: First, we show the result of one-step optimization applied to a nonelliptical target with $\delta = 0.1$. The estimated (x_0, y_0) center position of the estimated elliptical model, corresponding to the estimated translation motion, is illustrated by the dashed line in Fig. 4. The estimation accuracy is not high enough at $x = -0.2$ m and $x = 0.1$ m in this figure. Fig. 5 shows the actual and estimated rotation angles. Although the estimation is accurate at the beginning and the end, we see that the rotational angle
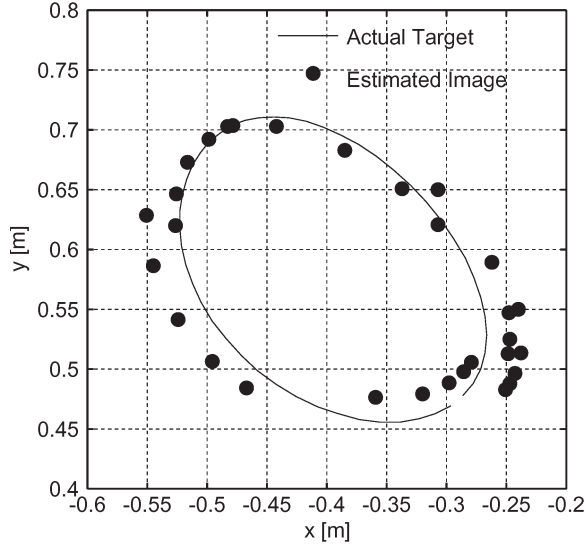
Fig. 6. Actual and estimated target shapes for nonelliptical target with one-step optimization method ($\delta = 0.1$).
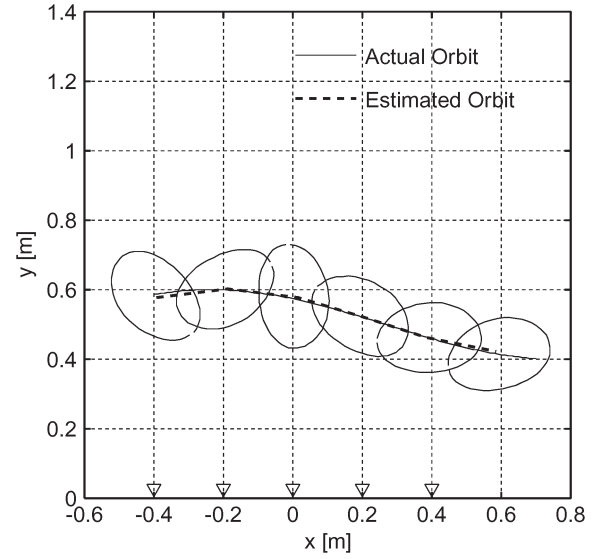

Fig. 7. Actual and estimated translation orbits with the two-step optimization method with fixed shape parameters ($\delta = 0.1$).
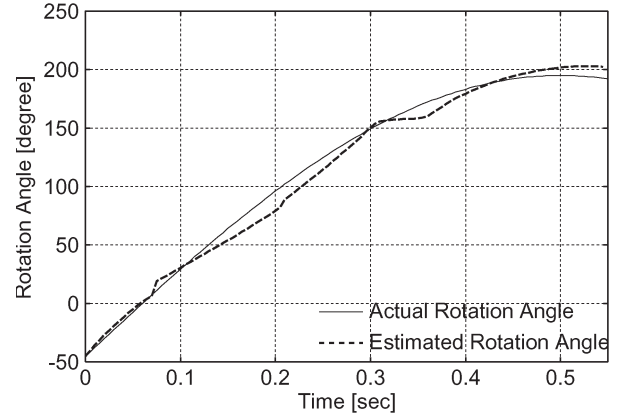

Fig. 8. Actual and estimated rotation angles with the two-step optimization method with fixed shape parameters ($\delta = 0.1$).

estimation becomes poor when the translation estimation is also inaccurate, giving a maximum estimation error of $25.8°$.

Fig. 6 shows the images of the actual and estimated shapes for $\delta = 0.1$ The entire shape is roughly estimated, but the accuracy is lower than that for the elliptical target. This is because the elliptical model is used for local fitting, although the target shape is not elliptical. The difference between the model and the actual target results in lowered accuracy. The root-mean-square (rms) error is 23.34 mm for the estimation. Note that the rms error ε is calculated by

$$\varepsilon = \sqrt{\frac{1}{N_a N_{\text{obs}}} \sum_{n=1}^{N_{\text{obs}}} \sum_{i=1}^{Na} \left(\hat{\boldsymbol{X}}_{n,i} - \boldsymbol{p}_{n,i} \right)^2} \qquad (17)$$

where $\hat{\boldsymbol{X}}_{n,i} = (\hat{X}_0^{(n,i)}, \hat{Y}_0^{(n,i)})$ is the point estimated using the ith antenna at the nth time step and $\boldsymbol{p}_{n,i}$ is the point on the actual target surface that is closest to the estimated point $\hat{\boldsymbol{X}}_{n,i}$.

3) Applying Two-Step Optimization: Next, we apply the two-step optimization method with fixed shape parameters to the same data for $\delta = 0.1$. The optimum parameters a and b are estimated using the quasi-Newton method with the initial values $a_{\text{init}} = 0.2$ m and $b_{\text{init}} = 0.2$ m. These initial values have been determined empirically, assuming that the target is part of a human body. The maximum peak is estimated to be $a = 0.146$ m and $b = 0.100$ m. These estimated values are close to the actual shape parameters $a = 0.15$ m and $b = 0.10$ m, for the elliptical model with $\delta = 0$. Although the assumed model is not identical to the ellipse, this algorithm can estimate the average parameters of a model.

Fig. 7 shows the actual and estimated translational motions using the two-step optimization method with fixed shape parameters. The actual and estimated translational orbits almost overlap, which means that the two-step method with fixed shape parameters can give a more accurate translation estimate than the one-step method in this case. Fig. 8 shows the actual and estimated rotational angles using two-step optimization with fixed shape parameters. It indicates some improvement

compared with the one-step method in Fig. 5. Fig. 9 shows the actual and estimated target shapes estimated using the two-step method with fixed shape parameters. The rms error of the image is 5.87 mm. The imaging accuracy is much higher than for the one-step optimization shown in Fig. 6. It can be seen that the time-averaging effect for estimating a and b is effective in stabilizing the entire estimating process for both the motion and shape of a target.

C. Application to a More Distorted Nonelliptical Target

Thus far, we have investigated the one- and two-step optimization methods with fixed shape parameters, applying them to elliptical and slightly distorted nonelliptical targets. In this section, we deal with a more distorted nonelliptical target to determine imaging performance under a more severe condition. We have confirmed that the one-step method does not work properly for any nonelliptical target. Consequently, we apply only the two-step method with fixed and variable shape parameters.

The assumed target shape is expressed by (16) with $\delta = 0.3$. The optimized shape parameters are $a = 0.181$ m and
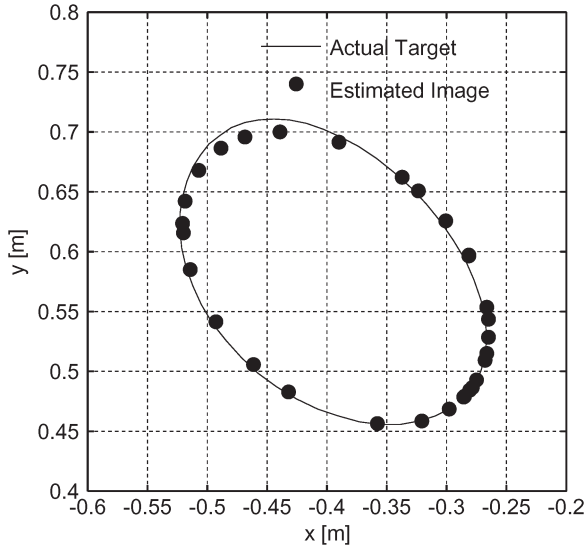
Fig. 9.   Actual and estimated target shapes using two-step optimization method with fixed shape parameters ($\delta = 0.1$).
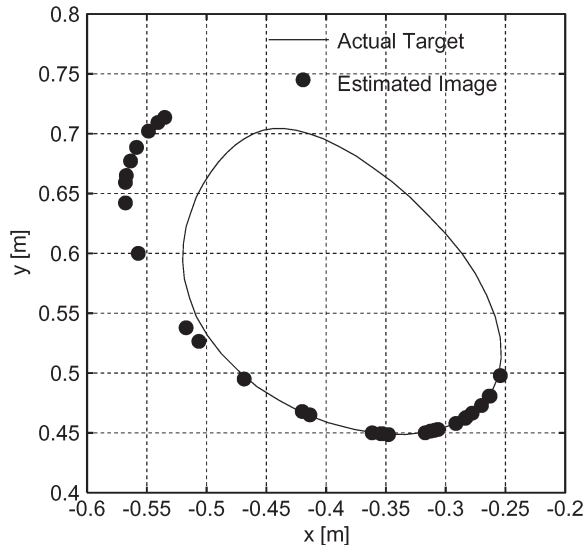

Fig. 10.   Actual and estimated target shapes using two-step optimization method with fixed shape parameters for distorted nonelliptical target ($\delta = 0.3$).

$b = 0.110$ m using the two-step method with fixed shape parameters. Fig. 10 shows the actual and estimated target shapes using the two-step method with fixed shape parameters. The image indicates a large error on the left side with no image points on the right side. The rms error for the image is 27.69 mm.

Next, we apply the two-step method with variable shape parameters. First, the smoothed $\bar{a}_n$ and $\bar{b}_n$ are estimated as the solid lines shown in Fig. 11. Here, the dashed lines are the $\hat{a}_n$ and $\hat{b}_n$ without smoothing, where $M = 56$ and $\sigma = 20$ ms have been empirically chosen. These values fluctuate around the basic shape parameters $a = 0.15$ m and $b = 0.10$ m. Fig. 12 shows the final image estimated using the two-step method with variable shape parameters. Although it has some points with error on the order of a few centimeters, the error is much smaller than that in Fig. 10. The rms error of the image is 7.70 mm. This shows that the two-step method with variable shape parameters is effective in obtaining an image of a distorted nonelliptical target. The difference between these two methods lies in the
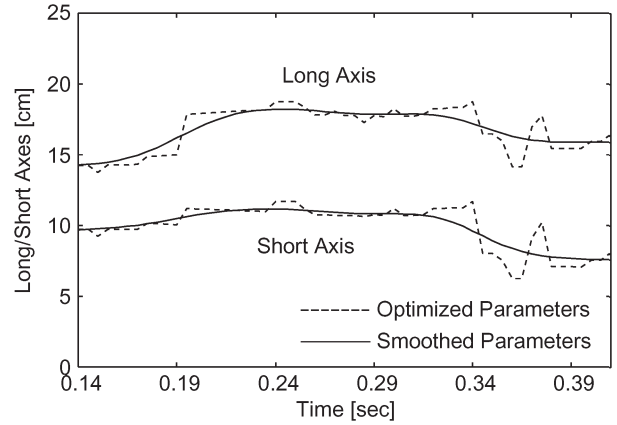

Fig. 11.   Estimated shape parameters $\bar{a}_n$ and $\bar{b}_n$ for distorted nonelliptical target ($\delta = 0.3$).
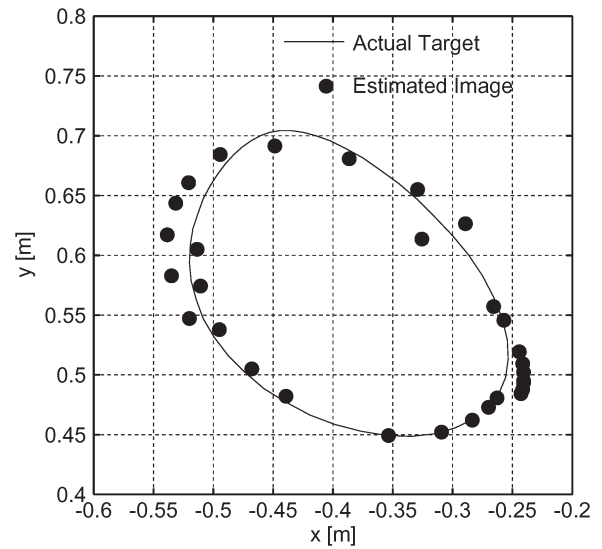

Fig. 12.   Actual and estimated target shapes using two-step optimization method with variable shape parameters for distorted non-elliptical target ($\delta = 0.3$).
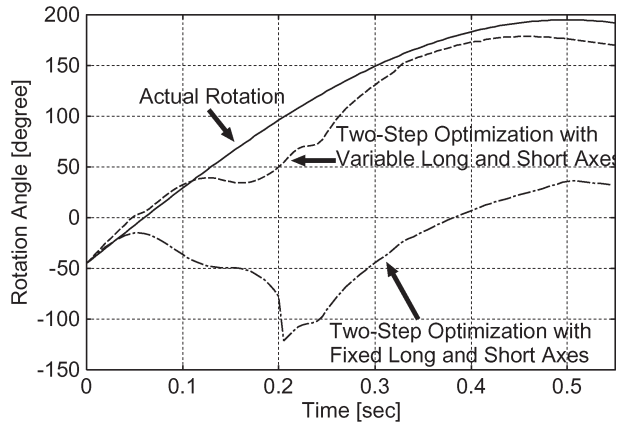

Fig. 13.   Actual and estimated rotation angles for distorted nonelliptical target ($\delta = 0.3$).

estimation accuracy of the rotational angle. The actual and estimated rotational angles are shown in Fig. 13, where the rotation estimated using the two-step method with fixed shape parameters has a large error for $t > 0.05$ s, which makes it difficult to obtain the right side of the target.
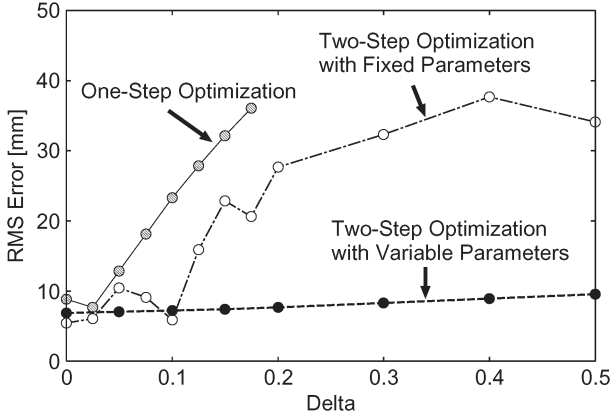
Fig. 14. RMS error of each method for a distorted nonelliptical target with parameter δ.

TABLE I
CALCULATION TIME FOR EACH PROPOSED METHOD

Method	Calculation time
One-step	0.8 sec
Two-step with fixed param.	4 sec
Two-step with variable param.	220 sec

V. NUMERICAL PERFORMANCE EVALUATION UNDER VARIOUS CONDITIONS

A. Performance Comparison of the Proposed Methods

Fig. 14 shows the rms error of images produced by the proposed methods. The target shape is expressed by (16) with the parameter δ. The figure demonstrates that the two-step optimization method with the variable shape parameters gives the smallest error even for a highly distorted target for $\delta > 0.1$. The two-step optimization method with the fixed shape parameters has the best performance for $\delta = 0$ because it assumes that the target shape is close to the ellipse. There is no plot for the one-step optimization method for $\delta \geq 0.2$ because the optimization process does not converge to produce any images.

Next, we compare the calculation time required for each optimization method. Table I lists the calculation times using a single Xeon 2.8-GHz processor. One-step optimization is the fastest followed by two-step optimization. Considering the rms errors, there is a tradeoff between the accuracy and the calculation time for the different methods. Therefore, it is necessary to determine the most appropriate method of the three for imaging, depending on the expected actual target shape.

B. Ranging Accuracy and Antenna Intervals Required for the Proposed Method

Next, we investigate the relationship of imaging accuracy, array size, and ranging accuracy. Fig. 15 shows the rms error of images obtained using the two-step method with fixed parameters for different antenna intervals Δx. An elliptical target shape and motion are assumed to be the same as in Section IV-A. The rms error values were calculated using a Monte Carlo simulation. Imaging error was calculated by adding white Gaussian random components to the simulated range $R_i(t)$
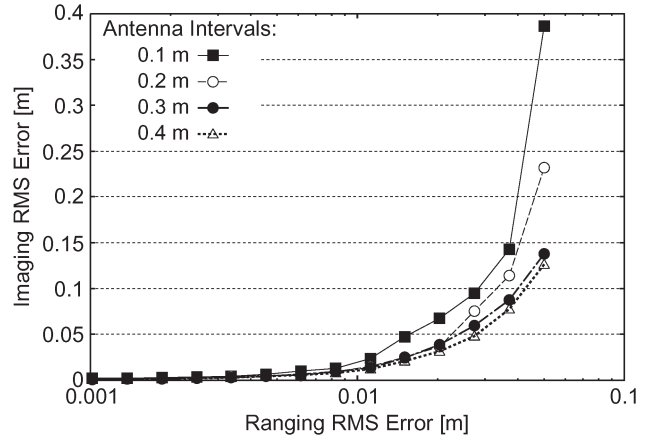

Fig. 15. Relationship between image error of the two-step optimization method with fixed parameters and ranging error for various antenna intervals.
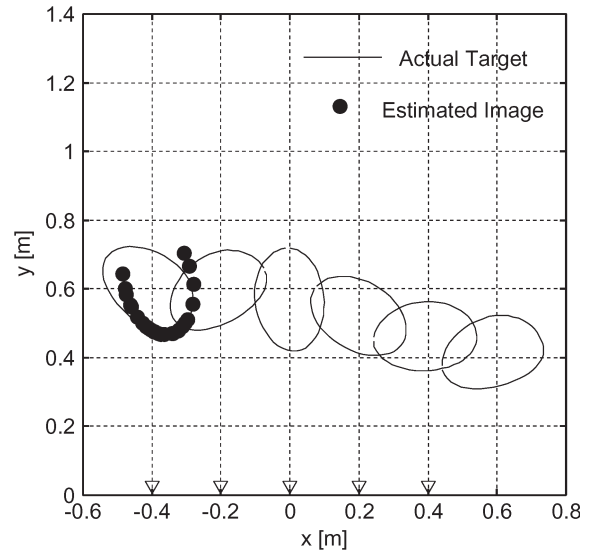

Fig. 16. Image generated using the two-step optimization method with fixed parameters for a time-variable target.

$(i = 1, 2, \ldots, 5)$ and applying the proposed method to the data. It is seen from Fig. 15 that, for our system model with $\Delta x = 0.2$ m, a ranging accuracy of 0.023 m is required to obtain an imaging rms error of less than 0.05 m. Similarly, ranging accuracies of 0.016, 0.024, and 0.028 m are required to achieve the same imaging rms error for $\Delta x = 0.1, 0.3$, and 0.4 m. This result indicates that it is advantageous to use longer antenna intervals to relax the system requirement for a specific ranging accuracy. However, a general conclusion cannot be drawn from this result because the actual imaging performance depends on many other factors such as target shape, translational and rotational motions, and antenna pattern. The important task now is to clarify these effects on imaging performance.

C. Application to Time-Variable Target Shape

Finally, we investigate how a time-variable target shape affects the imaging quality. We assume the distortion parameter δ to be time variable as $\delta(t) = \delta_0 + \eta t$ with $\delta_0 = -0.25$ and $\eta = 1.0$ s^{-1}. The target motion and antenna intervals are assumed to be the same as in the previous sections. The solid lines in Fig. 16 display the assumed target shape and motion,
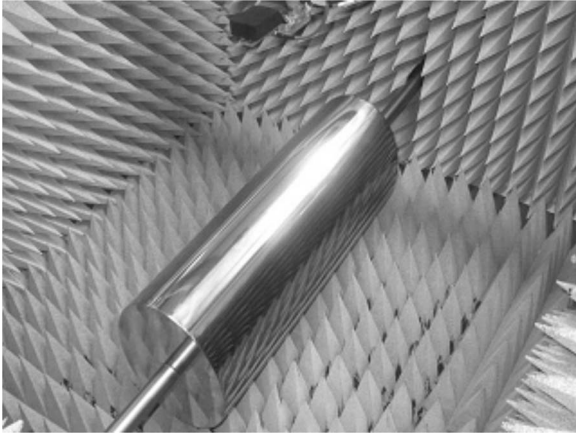
Fig. 17. Experimental site for UWB radar imaging.

Fig. 18. Measured signal with the center antenna with the experimental system.

where the target shape gradually changes. The estimated image using the two-step method with fixed parameters is illustrated in the figure with black dots. It is seen that the image has severely deteriorated because the proposed method assumes a fixed rigid target shape that does not match this model. Further modifications are necessary to apply the proposed method to a time-variable target like a human body.

VI. PERFORMANCE EVALUATION USING EXPERIMENTAL DATA

In the previous sections, we studied the applicability of the proposed method to distorted target shapes. The next step is to clarify the feasibility of the proposed method for measured data including the effects of realistic noise. In this section, we apply the proposed method to experimental data measured with the UWB system shown in Fig. 17. In this system, an elliptical cylinder in an anechoic chamber is held with thin bars on both sides. This cylinder is connected to an electronically operated rotation actuator. The antennas are scanned rather than the target itself because the received signals are identical to those assumed in this paper. Although this experimental setup is different from the system model explained in Section II, the measured data are the same as those measured with the assumed model. Note that this system is set up to simulate 2-D imaging data. Consequently, the antennas at the top of the figure are scanned in the direction perpendicular to the target cylinder.

The transmit and receive antennas are located close to each other and scanned together. The antenna interval d_a is 10.0 cm, which causes a systematic error in ranging because the system model assumes a monostatic antenna configuration in which d_a is zero. However, since the antennas are aligned in the length direction of a cylindrical target, the ranging error Δr can easily be eliminated using the Pythagorean Theorem given by $r = \sqrt{(r + \Delta r)^2 - (d_a/2)^2}$, where r denotes the actual range. These antennas have the UWB property of a 10-dB bandwidth of 3.0 GHz and a center frequency of 3.7 GHz. The antennas are ceramic patch antennas with a beamwidth that is wide enough to cover the target, which is not significantly different from the system model assumed for the computer simulation. A wideband impulse of 80.0-ps width is generated by a signal generator and input to one of the antennas, while the received
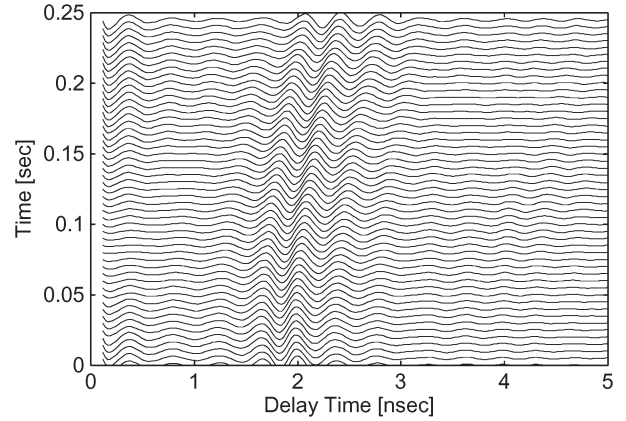
signal using the other antenna is amplified and A/D converted with a sampling oscilloscope. The digitized data are analyzed by the proposed imaging method.

The target has an elliptical cross section with long and short axes of $a = 0.15$ m and $b = 0.10$ m. The assumed motion is given by

$$X_T = X_0 + v_x t \qquad (18)$$

$$Y_T = Y_{T0} \qquad (19)$$

and the rotation is given by

$$\phi(t) = \phi_0 + \omega_\phi \qquad (20)$$

where $X_0 = -0.1$ m, $v_x = 1.0$ m/s, $Y_{T0} = 0.435$ m, $\phi_0 = -1.24$ rad, and $\omega_\phi = 3.5$ rad/s. The five antennas are located at intervals of 0.10 m.

Fig. 18 shows the signals received at the second antenna (the central one) under the conditions assumed previously. It is assumed that the signals are received every 5.0 ms. The signal-to-noise ratio (S/N) of the measurement data after applying the matched filter was 27.94 dB. First, we extract the peak points of each waveform to calculate $R_k(t)$. Note that this maximum detection is not optimal to estimate the delay time unless the filter is completely matched to the received waveform. At present, we are not considering the important task of employing a more accurate ranging technique [17] for this step in our methods.

We now apply the one-step method to the data and find that the method gives relatively large errors because of the noise components. Because the noise makes the optimization process strongly dependent on the initial value, the one-step method can be applied only to data with a high S/N.

Next, we apply the two-step method with fixed shape parameters to the experimental data. The estimated a and b are 0.156 and 0.099 m, respectively. These values are used to estimate other parameters. Fig. 19 shows the estimated rotational angle using the two-step method with fixed shape parameters. This figure shows that the proposed method works well even for the experimental data, although it does have an error of 5.6° at $t = 0.16$ s and 13.8° at the final step $t = 0.24$ s. Solid lines in Fig. 20 indicate the actual target shapes move to the right while rotating counterclockwise. Here, triangle symbols on the
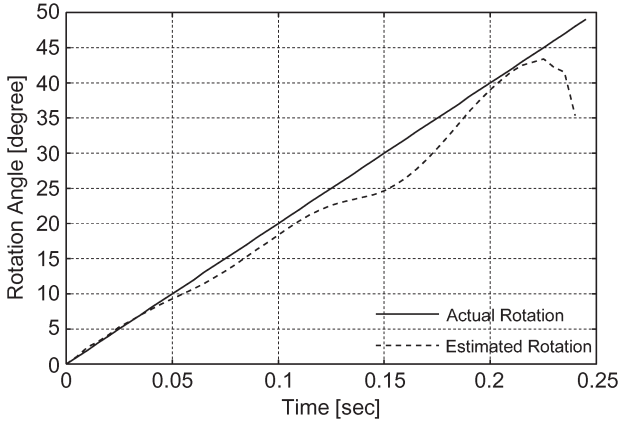
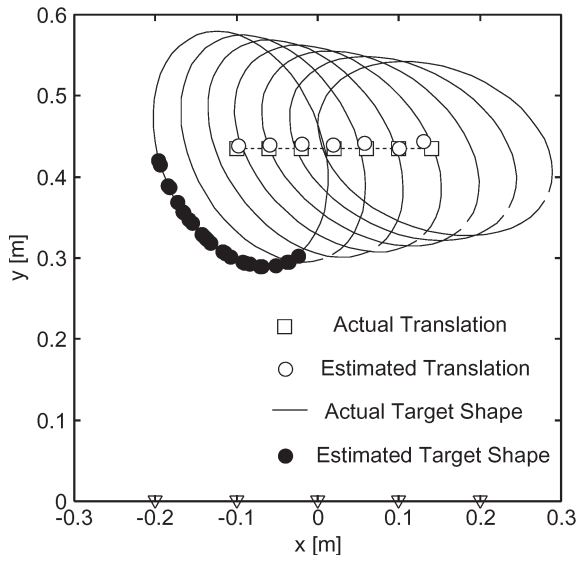Fig. 19. Actual and estimated rotation angles for experimental data.

Fig. 20. Target shape estimated by the proposed method for experimental data.

x-axis show the five antenna positions. An estimated image is displayed with black dots in Fig. 20 along with the estimated translation (x_0, y_0), which shows that the proposed method can accurately estimate the target shape with measurement data. The rms error of the image is 5.31 mm, which is small enough for most surveillance-related applications.

VII. CONCLUSION

We have proposed new imaging methods for UWB radar using five antennas. The methods use the motion of a target, including translation and rotation, to obtain a target image by compensating for the estimated motion. We presented three methods of optimizing the proposed cost function, the one-step optimization method, the two-step optimization method with fixed shape parameters, and the two-step optimization method with variable shape parameters. The one-step method works well for an elliptical target and works to some extent for a slightly distorted nonelliptical target, for which the two-step method with fixed shape parameters can accurately estimate the image. These two methods do not work well for a more dis-
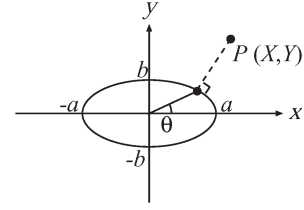
torted nonelliptical target, for which the two-step method with variable shape parameters works well. The two-step method with fixed parameters was also applied to experimental data to demonstrate its performance. Although the measurement conditions were idealized, assuming only an elliptically shaped target with simple motion, the proposed method was shown to be effective even for measured data.

APPENDIX

In this Appendix, we explain a procedure to obtain the foot perpendicular to the ellipse E from a point P outside the ellipse. To make the analysis easier, we set the spatial coordinates as follows: 1) the center of the ellipse is located at the origin, and 2) the long axis of the ellipse is on the x-axis.

Fig. 21. Estimated target shape with the proposed method.

The coordinate system is shown in Fig. 21. Let $\boldsymbol{X} = (X, Y)$ be the position vector of the point P. A point on the ellipse E is expressed by

$$\boldsymbol{v}(\theta) = \begin{pmatrix} a\cos\theta \\ b\sin\theta \end{pmatrix}. \tag{21}$$

Given the condition for perpendicularity

$$(\boldsymbol{X} - \boldsymbol{v}(\theta)) \cdot \frac{\partial}{\partial\theta}\boldsymbol{v}(\theta) = 0 \tag{22}$$

holds. By modifying this equation, we obtain

$$-aX\sin\theta + bY\cos\theta + (a^2 - b^2)\sin\theta\cos\theta = 0. \tag{23}$$

By introducing a variable $\tau = \sin\theta$, the equation can be rewritten as an equation of the fourth degree

$$A_4\tau^4 + A_3\tau^3 + A_2\tau^2 + A_1\tau + A_0 = 0 \tag{24}$$

where

$$A_0 = -b^2Y^2, \tag{25}$$
$$A_1 = -2b(a^2 - b^2)Y, \tag{26}$$
$$A_2 = a^2X^2 + b^2Y^2 - (a^2 - b^2)^2, \tag{27}$$
$$A_3 = 2b(a^2 - b^2)Y, \tag{28}$$
$$A_4 = (a^2 - b^2)^2. \tag{29}$$

Using Ferrari's solution for an equation of the fourth degree, we analytically obtain four solutions $\tau_1, \tau_2, \tau_3, \tau_4$. We choose a real solution from among them and calculate $\theta = \arcsin(\tau)$ to obtain θ. If multiple solutions are real numbers, we obtain multiple values for θ. In this case, we calculate the distance between $\boldsymbol{v}(\theta)$ and $\boldsymbol{X}$ for each solution to find the optimum solution. In this way, we obtain $\boldsymbol{v}(\theta)$ analytically.

REFERENCES

[1] L. Jofre, A. Broquetas, J. Romeu, S. Blanch, A. P. Toda, X. Fabregas, and A. Cardama, "UWB tomographic radar imaging of penetrable and impenetrable objects," *Proc. IEEE*, vol. 97, no. 2, pp. 451–464, Feb. 2009.

[2] C. J. Leuschen and R. G. Plumb, "A matched-filter-based reverse-time migration algorithm for ground-penetrating radar data," *IEEE Trans. Geosci. Remote Sens.*, vol. 39, no. 5, pp. 929–936, May 2001.

[3] A. G. Yarovoy, T. G. Savelyev, P. J. Aubry, P. E. Lys, and L. P. Ligthart, "UWB array-based sensor for near-field imaging," *IEEE Trans. Microw. Theory Tech.*, vol. 55, pt. 2, no. 6, pp. 1288–1295, Jun. 2007.

[4] T. Counts, A. C. Gurbuz, W. R. Scott, Jr., J. H. McClellan, and K. Kim, "Multistatic ground-penetrating radar experiments," *IEEE Trans. Geosci. Remote Sens.*, vol. 45, no. 8, pp. 2544–2553, Aug. 2007.

[5] S. Masuyama and A. Hirose, "Walled LTSA array for rapid, high spatial resolution, and phase-sensitive imaging to visualize plastic landmines," *IEEE Trans. Geosci. Remote Sens.*, vol. 45, no. 8, pp. 2536–2543, Aug. 2007.

[6] M. Dehmollaian and K. Sarabandi, "Refocusing through building walls using synthetic aperture radar," *IEEE Trans. Geosci. Remote Sens.*, vol. 46, no. 6, pp. 1589–1599, Jun. 2008.

[7] Y. Yang and A. E. Fathy, "Development and implementation of a real-time see-through-wall radar system based on FPGA," *IEEE Trans. Geosci. Remote Sens.*, vol. 47, no. 5, pp. 1270–1280, May 2009.

[8] X. Zhuge, A. G. Yarovoy, T. Savelyev, and L. Ligthart, "Modified Kirchhoff migration for UWB MIMO array-based radar imaging," *IEEE Trans. Geosci. Remote Sens.*, vol. 48, no. 6, pp. 2692–2703, Jun. 2010.

[9] T. Sakamoto and T. Sato, "Code-division multiple transmission for high-speed UWB radar imaging with an antenna array," *IEEE Trans. Geosci. Remote Sens.*, vol. 47, no. 4, pp. 1179–1186, Apr. 2009.

[10] Q. Huang, L. Qu, B. Wu, and G. Fang, "UWB through-wall imaging based on compressive sensing," *IEEE Trans. Geosci. Remote Sens.*, vol. 48, no. 3, pp. 1408–1415, Mar. 2010.

[11] Y. Matsuki, T. Sakamoto, and T. Sato, "Study of a method for 2-D imaging of simple-shaped targets with arbitrary motion using UWB radar with a small number of antennas," in *Proc. 20th Int. Conf. Appl. Electromagn. Commun.*, Sep. 2010, pp. 742–749.

[12] G. Y. Lu and Z. Bao, "Compensation of scatterer migration through resolution cell in inverse synthetic aperture radar imaging," *Proc. Inst. Elect. Eng.—Radar, Sonar Navig.*, vol. 147, no. 2, pp. 80–85, Apr. 2000.

[13] Z. Li, S. Papson, and R. M. Narayanan, "Data-level function of multilook inverse synthetic aperture radar images," *IEEE Trans. Geosci. Remote Sens.*, vol. 46, no. 5, pp. 1394–1406, May 2008.

[14] J. M. Muñoz-Ferreras and F. Pérez-Martínez, "Uniform rotational motion compensation for inverse synthetic aperture radar with non-cooperative targets," *IET Radar, Sonar Navig.*, vol. 2, no. 1, pp. 25–34, Jan. 2008.

[15] A. Aprile, D. Meledandri, T. M. Pellizzeri, and A. Mauri, "Translational rotational motion compensation: A single algorithm for different radar imaging applications," *IET Signal Process.*, vol. 2, no. 3, pp. 204–215, Sep. 2008.

[16] D. Marquardt, "An algorithm for least-squares estimation of nonlinear parameters," *SIAM J. Appl. Math.*, vol. 11, no. 2, pp. 431–441, 1963.

[17] S. Kidera, T. Sakamoto, and T. Sato, "High-resolution and real-time three-dimensional imaging algorithm with envelopes of spheres for UWB radar," *IEEE Trans. Geosci. Remote Sens.*, vol. 46, no. 11, pp. 3503–3513, Nov. 2008.

Takuya Sakamoto (M'04) received the B.E. degree from Kyoto University, Kyoto, Japan, in 2000 and the M.I. and Ph.D. degrees from the Graduate School of Informatics, Kyoto University, in 2002 and 2005, respectively.

He is an Assistant Professor with the Department of Communications and Computer Engineering, Graduate School of Informatics, Kyoto University. His current research interest is in imaging algorithms for ultrawideband radar and ultrasound systems.

Toru Sato (M'92) received the B.E., M.E., and Ph.D. degrees in electrical engineering from Kyoto University, Kyoto, Japan, in 1976, 1978, and 1982, respectively.

He is currently a Professor with the Graduate School of Informatics, Kyoto University. His major research interests include system design and signal processing aspects of ultrawideband radars and radar remote sensing of the atmosphere.